

#### **PAPER**

# A 3D helical filament surrogate model for 3D tokamak equilibria

To cite this article: Xuan Sun et al 2025 Plasma Phys. Control. Fusion 67 045028

View the article online for updates and enhancements.

## You may also like

- Improved scaling of the scrape-off layer particle flux width by the Bayes' theorem on EAST
  D C Liu, X Liu, L Wang et al.
- Integrated modelling of tokamak plasmas: progress and challenges towards ITER operation and reactor design C Bourdelle
- STORM modelling of scrape-off layer filament behaviour with hot ions S Ahmed, J T Omotani, S L Newton et al.

Plasma Phys. Control. Fusion 67 (2025) 045028 (16pp)

https://doi.org/10.1088/1361-6587/adc3c0

# A 3D helical filament surrogate model for 3D tokamak equilibria

Xuan Sun<sup>1,2,\*</sup>, Yueqiang Liu<sup>1</sup>, Lang L Lao<sup>1</sup>, Nathan Richner<sup>2</sup>, David Ryan<sup>3</sup> and Guoliang Xia<sup>3</sup>

- <sup>1</sup> General Atomics, San Diego, CA 92121, United States of America
- <sup>2</sup> Oak Ridge Associated Universities, Oak Ridge, TN 37830, United States of America

E-mail: sunxuan@fusion.gat.com

Received 3 February 2025, revised 14 March 2025 Accepted for publication 21 March 2025 Published 31 March 2025



#### **Abstract**

A novel approach for efficient representation of three-dimensional (3D) tokamak equilibria is investigated, where a set of helical current filaments occupying the plasma region are employed to resolve deviations from the two-dimensional (2D) axi-symmetric state. A discrete set of 3D filaments, located at rational surfaces for a given toroidal mode number n and following the 2D equilibrium field lines (thus forming closed current loops), are found to provide a surrogate model of 3D equilibria with reasonable accuracy. Specifically, application of the filament model to 3D perturbed equilibria, due to the resonant magnetic perturbation (RMP) in DIII-D and MAST-U discharges, reveals that (1) a single helical filament per rational surface is sufficient; (2) 21 such helical filaments are capable of representing the n = 2 3D response field in MAST-U with less than 10% relative error as compared to that computed by a full magnetohydrodynamic code; (3) optimizing currents (both amplitude and phase) flowing in 3D filaments with fixed geometry, the highest accuracy fitting is found to depend on the characteristics of the 3D equilibria such as the coil current phasing of the RMP coils in our case studies. This filament approach is also applicable for generating surrogate models of other type of 3D tokamak equilibria, including those during the initial phase of the plasma disruption.

Keywords: RMPs, surrogate modeling, filament model, equilibrium, perturbations, magnetic, MARS-F

#### 1. Introduction

Equilibrium reconstructions are crucial for understanding the internal plasma state which then impacts real-time plasma control as well as downstream physics analysis such as transport codes [1–5]. These reconstructions are obtained by solving the axisymmetric magnetohydrodynamic (MHD) force balance equation [6, 7]. Traditionally, the computed equilibrium constructions from codes such as EFIT [8] are two-dimensional (2D), assuming toroidal symmetry. The original development of equilibrium reconstruction codes started with reduced models that represented the toroidal current density with a series

of axisymmetric filaments [9, 10]. The resulting equilibrium quantities computed from these filament models were accurate representations of the original equilibrium they were approximating [10]. These filament models became the foundations that later led to 2D axisymmetric equilibrium reconstruction codes such as EFIT [8] which have been used extensively in understanding tokamak plasma physics since the codes' widespread adoption [1]. It is important to highlight that the axisymmetric filament approach is a developmental precursor to the eventual 2D equilibrium reconstructions since the filament model does not include key physics constraints such as force balance which is included in the full equilibrium reconstruction.

In present-day tokamak operation, it is known that the axisymmetric assumption of 2D equilibrium reconstruction

<sup>&</sup>lt;sup>3</sup> UK Atomic Energy Authority, Abingdon, Oxfordshire OX14 3DB, United Kingdom

<sup>\*</sup> Author to whom any correspondence should be addressed.

codes is not fully satisfied. Indeed, some examples such as the routine application of resonant magnetic perturbations (RMPs) for edge-localized mode (ELM) suppression and/or mitigation [11], as well as toroidally distributed magnetic measurements indicate that the plasma does not strictly follow toroidal symmetry. In general, these three-dimensional (3D, i.e. toroidally asymmetric) magnetic field responses have been small compared to the underlying 2D axisymmetric equilibrium and therefore have been regarded as perturbations. However, given the significance of these 3D magnetic response perturbations insofar as being used for ELM suppression as well as other instances such as 3D precursors to plasma disruption, 3D error fields, and more, it is important to better understand the 3D effects that are not contained within the traditional 2D axisymmetric equilibrium reconstruction algorithm. Furthermore, it is known that several tokamak discharges show increasing deviation from the axisymmetric equilibrium (as measured by increasing  $\chi^2$ ) as the discharge approaches a disruption. One potential explanation for this poorer axisymmetric equilibrium reconstruction is due to the increasing 3D effects that emerge close to disruption.

Originally motivated by the needs of the stellerator community which itself produces plasmas without toroidal symmetry in their equilibrium reconstructions, there have been several recent advances in 3D equilibrium reconstruction codes. Some of the codes used in present-day work include VMEC [12], V3FIT [13], STELLOPT [14], HINT2 [15], IPEC [16], GPEC [17], amongst many others (see [18] and references therein for more details). Furthermore, beyond the 3D equilibrium reconstruction, there are advances in 3D coil design in order to optimize key performance figures of merit such as in NESCOIL [19] and FOCUS [20]. The study presented in this paper is not a first-principles 3D equilibrium reconstruction code such as the aforementioned codes. Instead, it is a surrogate model that follows the original motivation of the 2D axisymmetric filament models. We demonstrate that this surrogate model is a proof-of-principle using numerical studies on 3D perturbed plasma response in order to provide a reduced order model of non-axisymmetric, helical filaments to represent the 'magnetic probe' measurements, tailored to the spatial distribution of magnetic field values. We note that this definition of a surrogate model is not the same as traditionally adopted since this model is more simplistic in implementation and, most importantly, does not obey key physics constraints such as force-balance which are present in modern equilibrium reconstruction codes. Instead, this model aims to provide a model-order-reduction by providing a physicallymotivated series of non-axisymmetric filaments to represent the magnetic probe measurements as plasmas gain 3D variations. Throughout this text, we use the term surrogate model to refer to this definition of a simpler, reduced order model. In this study, we develop and present a methodology of using 3D helical filaments as a surrogate model for a 3D nonaxisymmetric plasma equilibrium reconstruction, constrained by magnetic field values outside of the plasma, albeit without the force balance constraint. Similar work has been done using current filaments to model the plasma edge and scrape-off layer [21–24] and this work is distinguished by focusing on a simpler model with real-time computational implementation goals. This is a fundamentally physics-motivated surrogate model which is complementary to neural-network based surrogate models such as in [25].

When developing this type of reduced order surrogate model, we considered two different applications. First, we focused on RMPs which are typically used by modern day tokamaks for ELM suppression and mitigation [26]. Future generation machines such as ITER will also need ELM mitigation and suppression with plans to implement RMPs so therefore this model is applicable to next-generation devices [27]. It is important to note that not all next-generation machines will include RMPs and therefore this method may be of little use. However, the insights deduced from studies with this model may be useful in informing future design choices or give insights into leveraging limited information from reduced sets of magnetic probes. The RMPs create 3D perturbations on the plasma boundary and the resulting magnetic field response. The efficacy of RMPs on ELM suppression is related to this boundary perturbation [28] and thus having a proper way to estimate this perturbed plasma boundary would be helpful in evaluation and feedback of the applied RMP for its design purpose of ELM suppression. Second, this model can be used in plasma operation by assisting with disruption prediction and avoidance. In plasma operation, a disruption occurs when the plasma is sufficiently unstable and loses plasma confinement [29-31]. One typical indicator of imminent disruption is the appearance of 3D distortions in the plasma as a potential seed for further non-axisymmetric behavior and therefore eventual loss of confinement [32, 33]. These two applications provide burning plasma relevant modeling tools with the goal of deployment on next-generation machines.

The work in this paper is outlined as follows. In section 2, we provide a detailed description of the concept of the 3D helical filament surrogate model for non-axisymmetric plasma equilibrium reconstructions. In section 3, we apply the surrogate model to one particular application: the RMP. This application is performed for two different discharges—one from DIII-D and one from MAST-U, both with applied RMP but with different toroidal mode numbers. The perturbed 3D equilibrium response that is used for comparison is taken from MARS-F, a linear, resistive MHD simulation [34, 35]. Finally, in section 4, we conclude by describing the process to date, key takeaways from our early development of this algorithm, and a detailed description of the future direction in which we plan to develop this surrogate model.

#### 2. 3D helical filament model

In this section, we describe the algorithm that produces the 3D helical filament model. As described in the Introduction, the motivation for using this type of surrogate model is to build upon the initial work of the 2D axisymmetric equilibrium reconstruction's historical development by constructing 3D filaments that can reconstruct a non-axisymmetric equilibrium. It

is important to note that tokamak is mostly axisymmetric. We therefore use 3D filaments to represent 3D deviations from the 2D equilibrium. The latter is still associated with axisymmetric plasma currents which can be represented by axisymmetric filaments, if necessary.

There are, in principle, many different methodologies for choosing 3D helical filaments that would break toroidal symmetry. Our method is largely motivated by the fact that, according to the ideal MHD theory, the 3D plasma current perturbation is located at the mode rational surfaces forming current sheets [36]. Moreover, the most important current component is the one parallel to the equilibrium field lines since the parallel current component produces the perpendicular field perturbation (and as a result is responsible for screening the resonant field contribution), which is typically larger than the parallel/toroidal field component. It thus makes sense to choose helical filaments that follow the equilibrium field lines at certain rational surfaces. As an obvious advantage of such a choice, these helical filaments form closed loop geometries thus significantly reducing the complexity of the eventual surrogate model. For a given toroidal mode number n, the number of rational surfaces is finite (assuming equilibria with truncation at the plasma separatrix if the plasma contains an X-point). For each filament, the resulting B-field has a toroidal mode number n distribution but for this work, to compare with MARS-F results, we use only a single selected toroidal mode number field component for comparison. An interesting question, which we will answer with the present study, is the number of filaments needed per rational surface. We note that while MARS-F itself is not a full 3D equilibrium code capable of computing non-linear effects, it will suffice for the purposes of this proof-of-principle study. Namely, we will be able to get physical simulations of 3D perturbations for the magnetic field outside of the plasma boundary which the helical filaments (described below) are going to try to reproduce. For the full machinery of 3D equilibria, other codes are available but MARS-F has been validated against specific applications of those codes [37].

We note that the radial location of 3D current perturbations is often more complicated than the ideal MHD prediction. For instance, (i) finite plasma resistivity results in volumetric current distribution near the rational surface instead of the surface current sheet in the ideal case; (ii) when a rotating plasma responds to a static RMP field or a MHD instability occurring in a rotating plasma is locked to the resistive wall, multiple current sheets form near but not exactly at the mode rational surface due to the so-called resonant splitting effect [36]. All these higher-order effects are neglected in our 3D filament model.

The set-up of this 3D helical filament model is described as follows and each step is expanded upon further below:

- (i) Plasma equilibrium: obtain the 2D axisymmetric plasma equilibrium which determines the magnetic flux surfaces
- (ii) Start filament trace: determine one or multiple filaments set at each rational q-surface. Multiple filaments are

- distributed uniformly along the poloidal coordinate  $\theta$  for a given q-surface.
- (iii) Determine filament geometry: field-line tracing code gives closed helical filaments when initiating the filament on a rational *q*-surface.
- (iv) Compute basis filament response: give each 3D helical filament 1 kA of current and compute their magnetic field response at desired locations. These are used as basis responses with (complex) coefficients that are fitted to the (synthetic) data.
- (v) Optimize filament currents: using reference data at the magnetic field response locations, construct a system of equations and optimize (i.e.  $\chi^2$  minimization) the (complex) currents flowing in the 3D helical filaments.

In the first step, (i) we obtain a 2D axisymmetric plasma equilibrium which we use in determining the filament geometry. For this work, a kinetic equilibrium was used but, in principle, any equilibrium which can produce flux contours that yield closed geometries would be sufficient. (ii) In the next step, we determine the filament geometry by choosing different flux surfaces on which to start a filament. These can be started by indexing a flux coordinate (i.e.  $\rho$ ) and located throughout the poloidal cross-section of the plasma by giving a poloidal coordinate  $\theta^4$ . Either a single filament can be used for each rational q-surface or multiple filaments which we choose to uniformly distribute along a rational q-surface, indexed by poloidal angle  $\theta$ . The final model procedure uses only a single filament without loss of generality (see discussion further below). (iii) For the third step, we determine the filament geometry by using a field-line tracing code which takes the 2D axisymmetric equilibrium as input. For this study, we used a module of the MARS-F code called REORBIT [38], an extension to MARS-F that simulates the trajectory of energetic electrons under the influence of the plasma field. A low-energy electron starting on a rational q-surface is used to approximate our filament geometry. In principle, and for future use cases, this step can be replaced with any procedure that can compute a field-line trace to represent the filament geometry. For our study, REORBIT was sufficient for our use case and we note the filament geometry only needs to be computed a single time. (iv) In the fourth step, we compute the magnetic field response at pre-determined locations. The magnetic field response at these locations is computed using a simple Biot-Savart calculation:

$$\mathbf{B}(\mathbf{r}) = \frac{\mu_0}{4\pi} \int_C \frac{Id\mathbf{l} \times \mathbf{r'}}{|r'|^3} \tag{1}$$

where  $\mu_0$  is the magnetic vacuum permeability, **l** is a point along the wire,  $\mathbf{r'} = \mathbf{r} - \mathbf{l}$  and **r** is the point we want to compute the magnetic field. These magnetic field responses at the collection of points  $\mathbf{r}_i$  form the response due to the basis filaments and since the Biot–Savart equation is linear, these field

<sup>&</sup>lt;sup>4</sup> In order to calculate the  $\rho$  that corresponds to each rational q-surface, we perform a cubic spline interpolation where a q-profile is given as input and the desired q values are taken as output from the interpolation.

response values can be multiplied by a complex current in the optimization step. (v) Finally, in the fifth step, we perform an optimization to determine the value of these complex current coefficients in each 3D helical filament. The optimization employed in this work is a simple least-squares minimization and defined as follows:

$$Ax = b \tag{2}$$

where A is a  $3N \times M$  matrix and N is the number of probe points we are interested in computing, M is the number of filaments available, x is a vector of M size, and b is a vector of 3N size. A is computed by taking the magnetic field response due to all individual filaments in the 3D helical filament model and computing their magnetic field response at the probe locations. These form the columns of A. b is the magnetic field response at those same probe points given by MARS-F, which already removes the larger axisymmetric component as described in the previous section. x is a vector of the complex current coefficients and determined by a least-squares fit. The resulting best fit complex currents yield the best matching magnetic field responses at each position compared to the data at those same positions. In principle, those data can and should be magnetic probe measurements during real-time deployment but for this work those data are the results from a MARS-F 3D magnetic field simulation for ease of interpretation, development and validation of the algorithm. In experiments, the probes would have to contain a toroidal distribution in order to identify a distinct toroidal mode number n. However, in the MARS-F simulations, the solutions have a given toroidal mode number n so such a probe distribution is not necessary.

Once the optimized filament currents are obtained, the residual values can also be computed. Since each filament is a complex current, the magnetic field response is also complex at the probe locations. There are multiple ways to define a residual here. Our formulation is as follows:

$$\operatorname{Res} = \frac{1}{N} \sum_{i=1}^{N} \frac{\int \frac{(B_{\operatorname{fil},i} - B_{\operatorname{Mars},i})^{2}}{B_{\operatorname{Mars},i}^{2}} \times w(\theta) d\theta}{\int w(\theta) d\theta}$$

$$\Longrightarrow \frac{1}{N} \sum_{i=1}^{N} \frac{(B_{\operatorname{fil},i} - B_{\operatorname{Mars},i})^{2}}{B_{\operatorname{Mars},i}^{2}}, \text{for } w(\theta) \equiv B_{\operatorname{Mars}}(\theta)^{2}$$

$$(4)$$

where  $B_{\mathrm{fil},i}$  represents the magnetic field response from the filament model for the ith field component,  $B_{\mathrm{Mars},i}$  is the same for the MARS-F magnetic field response, and  $i \in \{\mathrm{real}(B_{\mathrm{fil},R}), \mathrm{imag}(B_{\mathrm{fil},R}), \mathrm{real}(B_{\mathrm{fil},Z}), \mathrm{imag}(B_{\mathrm{fil},Z})\}$ . That is, the field components are both the real and imaginary contributions from each in-plane orthogonal field component. In the equation (3), we represent the fractional residual equation with a weight over the poloidal angle coordinate,  $\theta$ . In principle, different choices of weight functions,  $w(\theta)$ , correspond to different relative error functions. In this study we choose  $w(\theta) = B_{\mathrm{Mars}}(\theta)^2$  which emphasizes larger signals and results in equation (4). Other conventional choices include  $w(\theta) = 1$  and results in the conventional relative error estimate. The

overall choice of exact weighting function is dependent on the use-case of this helical filament model. Finally, we note that in our calculations of the residual, we provide the average fractional residual which normalizes over the number of magnetic field components used in the residual computation. As mentioned earlier, there are many ways to define a residual error metric. This is the chosen method for this study in order to roughly quantify the trends as we make changes to the helical filament surrogate model algorithm. In future implementations of this model, the error metric can be modified or redefined in order to better suit the particular experimental system (and associated magnetic sensors) that are being used in the helical filament computation.

This particular algorithm for developing the 3D helical filament model contains some advantages, one of which we highlight here. That is, the linearity of each step in the model development. Since the Biot-Savart calculation is linear and the filament geometry is pre-determined at this step, the entire process is maximally parallelizable. Namely, each filament current segment can compute its individual contribution to the magnetic field response with known geometry independently and in parallel. This implies that this algorithm has a lot of upside when implementing this model for distributed computing systems with GPU parallelization and potentially performing real-time modeling to assist with plasma operations and control. In this work, we performed the initial development of the algorithm and model on a personal laptop using a 11th Generation Intel i7 core CPU. Therefore, we did not have any considerations for optimizing the run-time. However, we note that in future use cases, the algorithm lends itself to highly optimized parallel computations.

When developing this type of reduced order surrogate model, we considered a few different applications such as the RMP and 3D precursors to disruption, as discussed in the Introduction. The RMP was the majority of the focus of this work and the surrogate model presented in this study aims to reconstruct 3D equilibria in the presence of distributed magnetic probe measurements<sup>5</sup>. The procedure developed here would also be able to determine fast reconstructions of 3D equilibria which, coupled with the computational speed-ups described previously, could be used as a tool to assist with plasma operations. In the initial stages of developing the surrogate model algorithm, we focused on the magnetic field response and run-time simplicity in order to better generalize to existing MARS-F simulations and leave room for further development into different use cases.

# 3. Application of filament model to perturbed 3D equilibria due to RMPs

As a first application of this 3D helical filament model, we validate against the computed perturbed 3D field that has an

<sup>&</sup>lt;sup>5</sup> In practice, we use a planar distribution of simulated magnetic measurements taken from MARS-F because the toroidal dependence of the solution for a given toroidal mode number *n* is analytically assumed.

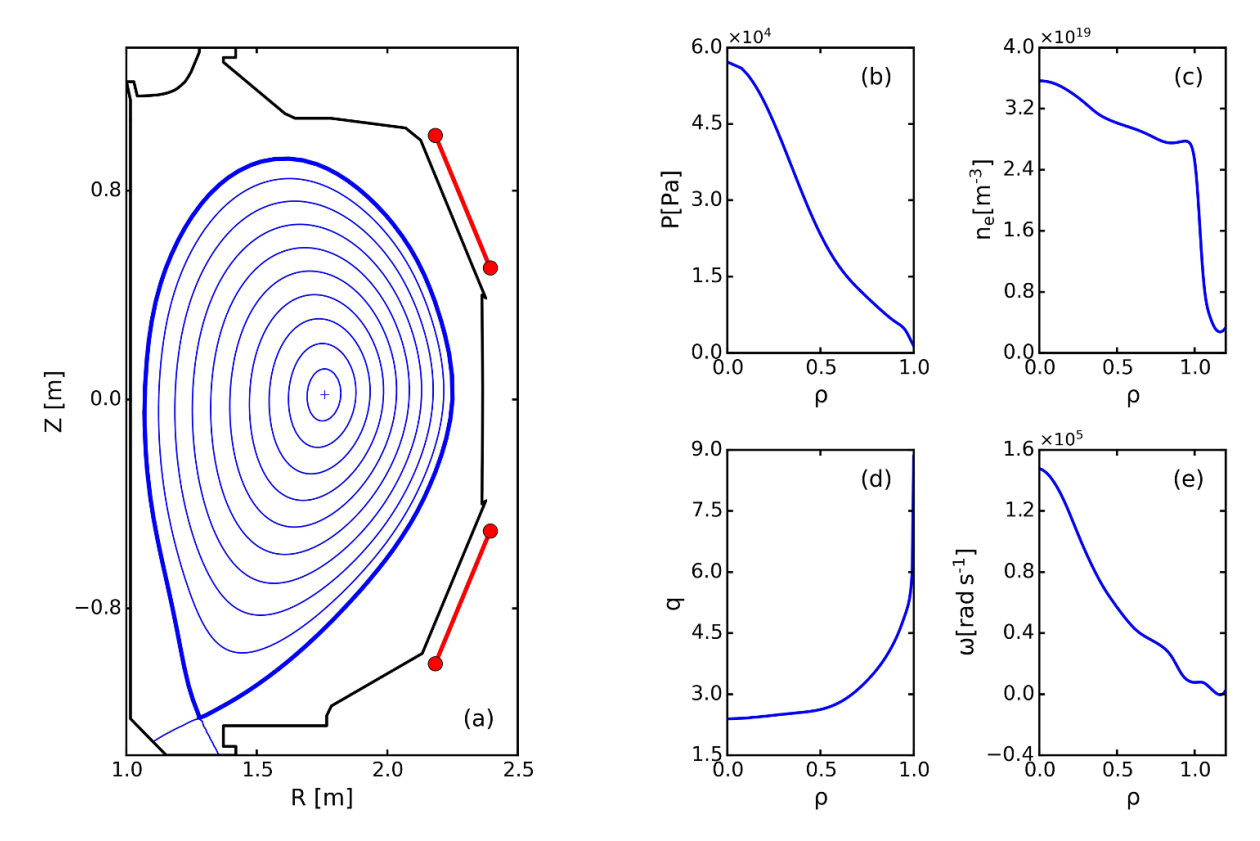


**Figure 1.** Several relevant equilibrium quantities used in this 3D helical filament model validation using a DIII-D discharge. The panels show (a) the 2D equilibrium flux contours (blue) with the DIII-D limiter (black) and the upper and lower I-coils (red) overlaid; (b) the pressure profile; (c) the electron density profile; (d) the *q*-profile; and (e) the rotation profile as measured by the carbon impurity rotation [44, 45]. This equilibrium comes from discharge 153485 at 850 ms.

RMP. The perturbed equilibrium response was obtained with MARS-F. We perform this validation for two different discharges from two different tokamaks: DIII-D with conventional aspect ratio and MAST-U with tight aspect ratio. The toroidal mode number of the solution is fixed which then leaves a finite number of rational q-surfaces. For DIII-D the toroidal mode number n was 1 and for MAST-U the toroidal mode number n was 2.

#### 3.1. DIII-D discharge with n = 1 RMP

The DIII-D tokamak is a conventional aspect ratio tokamak located in San Diego, California, USA. It has a rich history in plasma physics contributions and has been described extensively in [39–41] (and reference therein). For the purposes of this work, we mainly consider DIII-D discharges with applied RMPs which are done by driving current through window-frame coils in the upper and lower plane of the tokamak. These are called the I-coils and are conventionally used for RMPs for ELM suppression and mitigation on DIII-D [11]. For DIII-D, discharge 153485 was used [42]. This discharge has applied RMP for ELM mitigation and MARS-F simulation results for this discharge have previously been validated [35].

In order to build the 3D helical filament model, we follow the procedure described in section 2. For this

DIII-D discharge, the equilibrium reconstruction and profile information was obtained using the kineticEFITtime module contained within the OMFIT framework [43]. The resulting equilibrium flux contours and relevant profiles are shown in figure 1.

Using the flux contours from this equilibrium reconstruction, we can start field-line traces from different rational *q*-surfaces and in our study we use a code called REORBIT, a module in MARS-F, for this field-line tracing. A single filament corresponding to each rational *q*-surface is used in the 3D helical filament model. We note that multiple filaments for each rational *q*-surface was also investigated but, for reasons discussed below, ultimately were not used in the final surrogate model. Several basis filament geometries for the DIII-D discharge are shown in figure 2. We observe that at high-helicity, the filaments linger and show more structure at the X-point for this single-null plasma.

In each panel of figure 2, we show one closed helical loop. The filaments themselves have traces that go close to the limiter on the low-field side of the tokamak, outlined in black. These near trajectories create localized hot spots in the *B*-field response which is located close to the limiter as well (see below).

Next, we obtain the magnetic field response at a specific set of 3D locations. For this study, we took 512 probe points

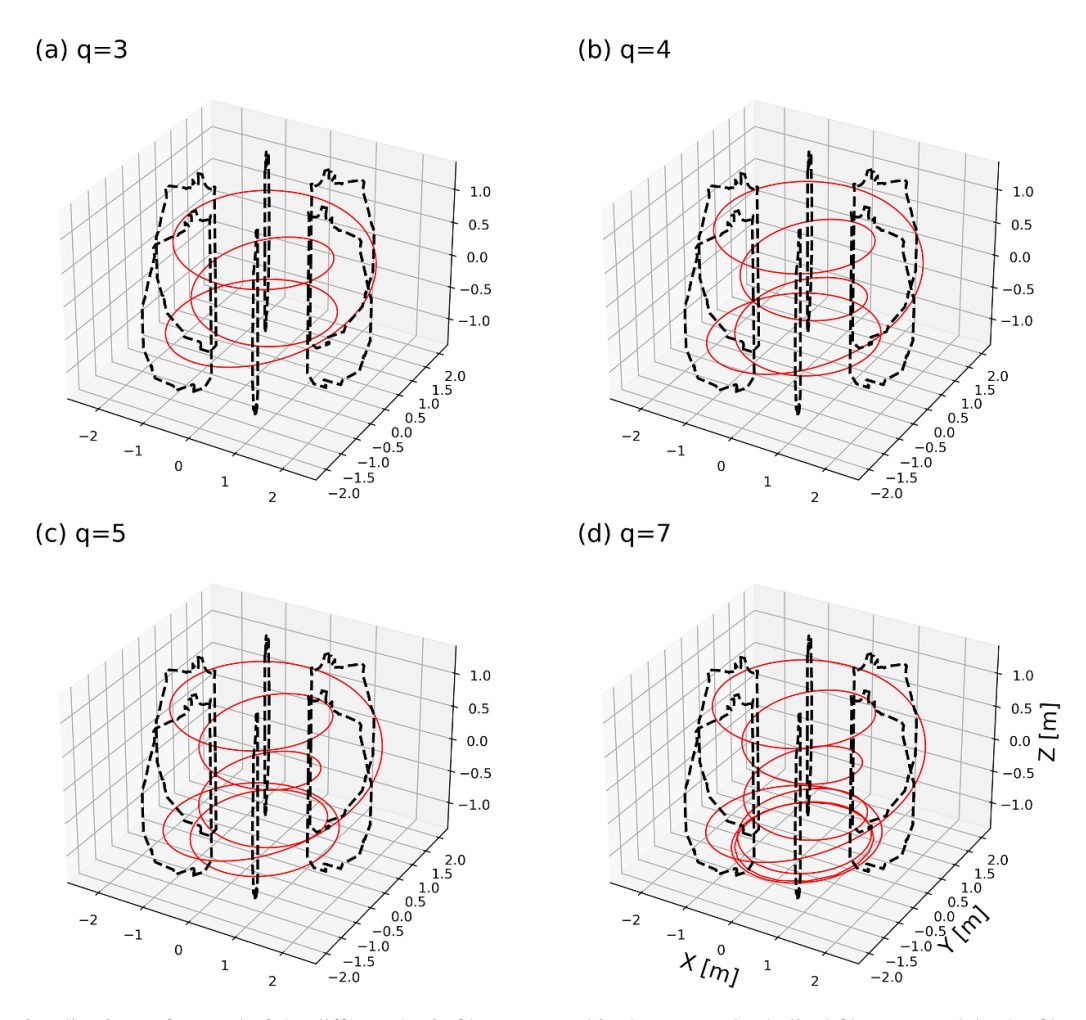


**Figure 2.** 3D visualizations of several of the different basis filaments used in the DIII-D 3D helical filament model. The filament geometry is obtained using REORBIT to perform a field-line trace, starting from a rational q-surface. In each subfigure, we show the geometry (red) corresponding to different q values: (a) q = 3, (b) q = 4, (c) q = 5, and (d) q = 7. The limiter is shown at six different toroidal slices (dashed black).

distributed uniformly along a surface called the 'resistive wall' in MARS-F, set at toroidal angle  $\phi = 0$  since the  $B_{\phi}$  component of the MARS-F solution is analytic. In this context, the 'resistive wall' is not the typical resistive wall of the tokamak device. Instead, it is a surface indexed by poloidal angle  $\theta$  which matches the plasma boundary surface and is extended outwards to approximately align with the device resistive wall. The purpose of this surface is to provide a smooth surface outside the plasma at a physically-relevant location (for future implementations of this model, the magnetic probes are located at the resistive wall) in order to extract the simulation results. The surrogate model gives each filament 1 kA current for these magnetic field response calculations. We note that the procedure is generalizable to 3D probe locations but for ease of comparison to MARS-F simulation results and initial development of the procedure, all the magnetic probe values are taken in the (R,Z) plane. Future work will investigate comparisons to magnetic probes that are toroidally distributed to identify individual toroidal n components. For this work, it is sufficient to select a specific toroidal n number because

the MARS-F simulation computes solutions with a given toroidal n.

The *B*-field is computed by the surrogate model using equation (1). Figure 3 shows the locations and predicted magnetic field response at 76 magnetic probe locations, which are the same probes given as input into the EFIT code [46, 47]. The DIII-D inner limiter surface and the MARS-F resistive wall surfaces are also outlined. The field strength is given with a corresponding color bar.

As was alluded to earlier, we performed an intermediate study throughout the course of this work. Initially, our procedure for the 3D helical filament model used multiple filaments starting from a uniform poloidal distribution along the same q-surface. Conceptually, each filament should represent an additional degree of freedom that could be used in the overall optimization. When we examined the resulting magnetic field response, we found that each basis filament's response looked identical up to a rotation, for basis filaments on the same rational q-surface. In figure 4, we show the 2D heatmap magnetic field response of multiple different basis filaments

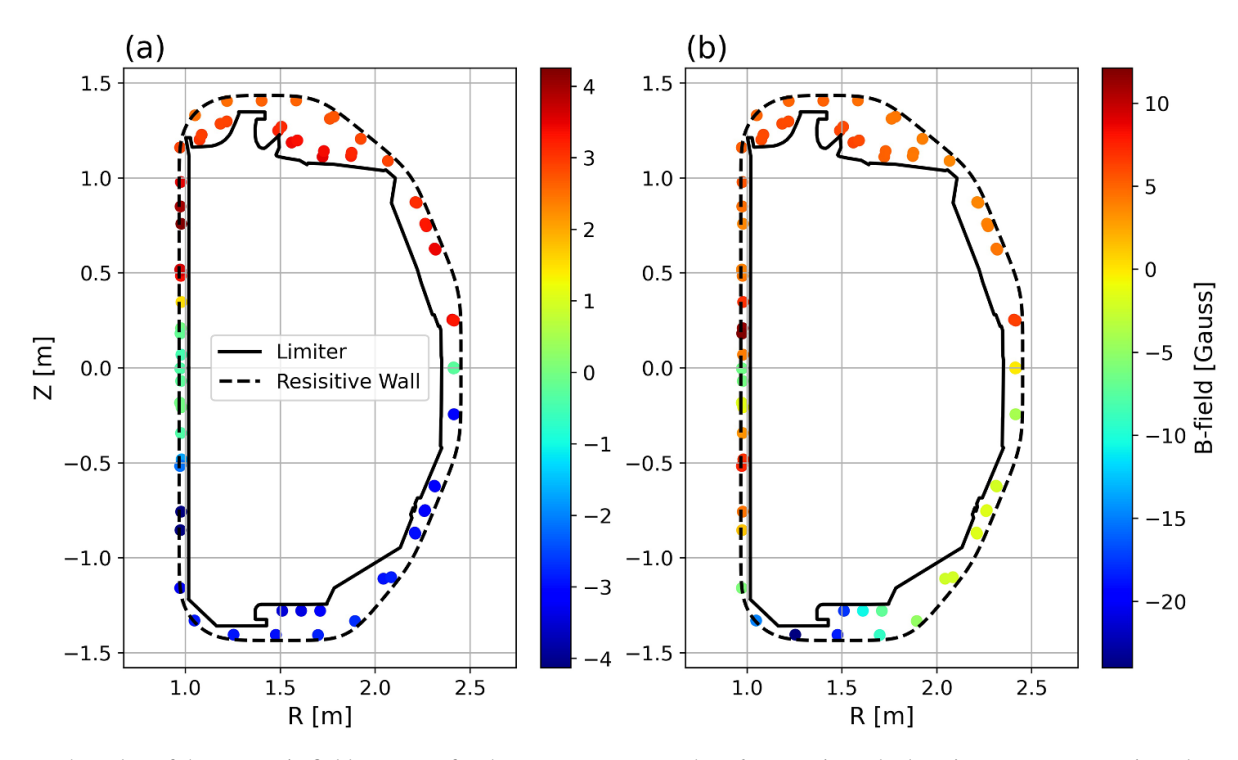


Figure 3. The value of the magnetic field response for the  $B_R$  component at the 76 magnetic probe locations on DIII-D projected onto the coordinate RZ-plane. Similar to EFIT, the probes are taken in-plane at an arbitrary toroidal angle  $\phi$  (when comparing with MARS-F). A single filament with 1 kA current produces this magnetic field for each panel. The filaments are denoted by their corresponding q-surface: (a) q = 3, and (b) q = 7. The limiter (solid black) and resistive wall (dashed black) are also shown.

(i.e. with a given 1 kA current). The 2D response is given in toroidal angle  $(\phi)$  and poloidal angle  $(\theta)$ . The  $\phi$  dependence of the field is taken to be analytical with the exponentiated factor  $e^{in\phi}$  where n is the toroidal mode number, following the same form as the MARS-F solution. To each panel of figure 4, we applied a different rotation in the toroidal coordinate which corresponds to a cyclic translation along the horizontal axis. This yielded visually identical field responses. This can be intuitively understood since q represents the ratio of toroidal and poloidal turns of the field-line and therefore different starting locations have the same behavior around the torus—simply offset by a rotation factor that would align the poloidal angles of different filaments along the same rational

These results have implications for our 3D filament model. Most notably, because each filament's magnetic field response is the same up to a (complex number) factor, that implies they are all linearly dependent. As a result, there is a maximum number of closed helical filaments that can be used and therefore a maximum number of degrees of freedom in the fit. This number can be quite low for low toroidal mode numbers-for our DIII-D discharge, we have only five total linearly independent filaments when constraining n = 1. This also implies a form of model-order-reduction. An arbitrarily large number of filaments with infinitesimal current can be distributed uniformly along the poloidal angle of a rational q-surface, creating a current sheet as predicted by the ideal MHD theory. However, figure 4 shows that all contributions of multiple filaments, located on the same q-surface, are linearly dependent. Assuming an array of such filament currents  $I_i$ , where  $j = 1, \dots, M$ , the resulting field perturbations can be written as  $\delta B_i = \delta B A_i e^{i\phi_j}$  where  $\delta B$  is the 'basis' field. The total field is thus

$$\delta B_{\text{total}} = \sum_{j=1}^{M} \delta B_{j}$$

$$= \delta B \sum_{j=1}^{M} A_{j} e^{i\phi_{j}},$$
(6)

$$= \delta B \sum_{i=1}^{M} A_j e^{i\phi_j}, \tag{6}$$

where the last summation just produces a scalar complex number. The above shows that the field produced by an array of current filaments (located on the same rational surface) can be represented by that from a single filament. We note that equation (5) is general with complex currents but in the instance of figure 4, a real 1 kA current is given to the filament and the magnetic field response shown is for the associated real-valued current. We also note that this description of the filament model is very reductive—it lacks the potential to describe complicated current distributions within the plasma. In fact, a filament geometry described above yields simplistic representations that will, for example, trace through associated X- and O-points in the magnetic topology which may or may not be relevant for the underlying plasma current distribution. As well, more detailed studies of the magnetic topology such as magnetic island chains, while available for the

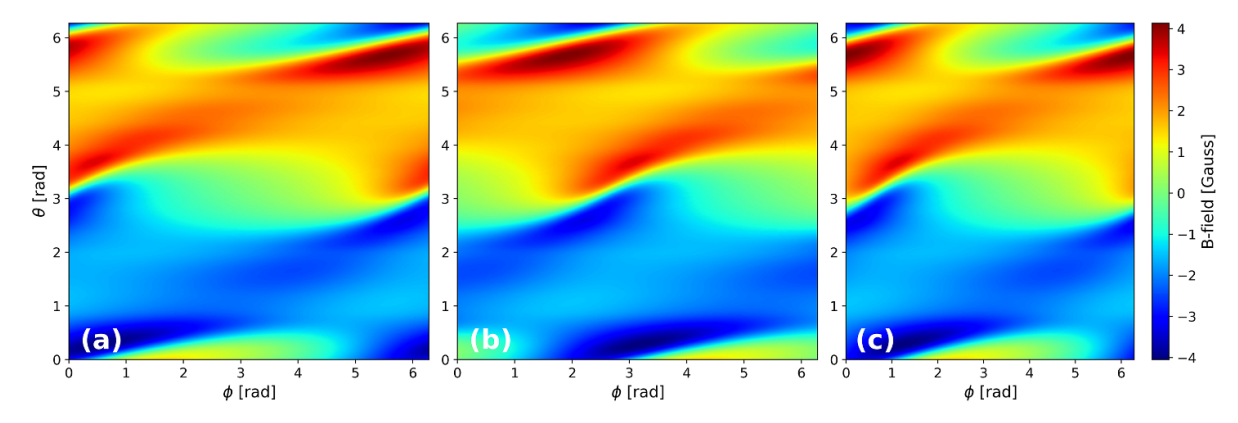


**Figure 4.** Magnetic field response,  $B_R$  component, for three different filaments that are all initiated on the same rational q-surface: q = 3. There were nine total filaments uniformly distributed along poloidal  $\theta$  angle in this study and a subset of three are shown in panels (a), (b), (c). The poloidal angle  $\theta$  traces out the resistive wall and the toroidal angle  $\phi$  is uniformly distributed around the DIII-D torus.

MARS-F response that is used in the comparison, are less relevant for the filament model due to the current distribution producing infinite field perturbations at the rational surfaces due to the near-field effect. The filaments themselves are meant to represent the shielding current sheets formed in ideal plasma response and the ideal response is not capable of reproducing magnetic islands. Instead, we re-iterate that this model is meant to be a reduced-order-model that can quickly capture a representation for the plasma that reproduces the magnetic probe measurements and, in real-time deployment, can quickly compute magnetic field values at other external 3D locations once the methodology is validated (such as in this proof-of-principle work). For this reason, we are less interested in the magnetic topology as compared to magnetic field values outside the plasma boundary where hypothetical probes would exist (in this work we use a 'probe' surface since it is set within MARS-F).

In this study, our methodology presents comparisons between the complex-valued currents and complex-valued magnetic field responses. These complex-values naturally arise due to comparing the various Fourier toroidal mode numbers of the magnetic field response with those extracted from MARS-F. This is because the MARS-F response computed is given for a given toroidal mode number response. In order for a comparison to be made, the helical filament model then computes the magnetic field response in 3D space and performs a Fourier mode decomposition for the magnetic field response, yielding a complex-valued response. In order to study the toroidal sideband effects i.e. the non-dominant toroidal mode numbers, we investigate the components of the magnetic field response for different toroidal n values for the DIII-D discharge. A single filament which is instantiated at q=3 produces a magnetic field response and is shown in figure 5. Some initial features stand out. Namely, the majority of the response structure is located at the midplane on the high-field side and smaller structures located at the lowfield side. In terms of amplitude, the dominant toroidal mode number (n = 1 for this DIII-D discharge with applied n = 1

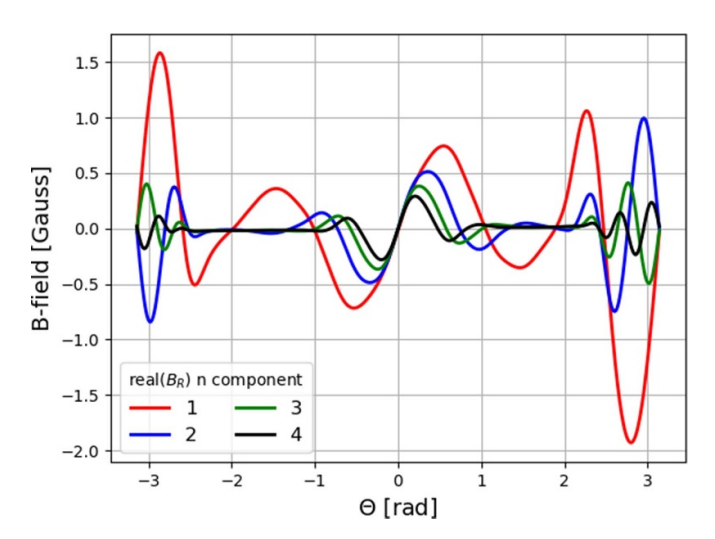


**Figure 5.** Magnetic field response of the DIII-D discharge q=3 helical filament as a function of the poloidal angle  $\theta$  as it traces the contour of the 'resistive wall' (see text for detailed definition). The magnetic field response shown is the real component of the  $B_R$  field for 4 different Fourier decomposition toroidal mode numbers. The current in this filament is 1 kÅ.

RMP) is largest with each subsequent Fourier mode number n decreasing in overall amplitude. This indicates that the sideband effect is important but that capturing the dominant toroidal mode number still models the most important features. When this type of model is implemented in experiment, a Fourier decomposition will likely not be possible due to limited toroidal resolution of the magnetic measurements. In those instances, this tool will simply be used to reconstruct real-valued filaments to capture the model-order-reduced currents that reproduce the magnetic probe measurements. However, at the current stage of study, the flexibility in the helical filament model to extend the coverage of the magnetic field response in 3D allows for systematic studies to better understand the nuances of the magnetic field response such as

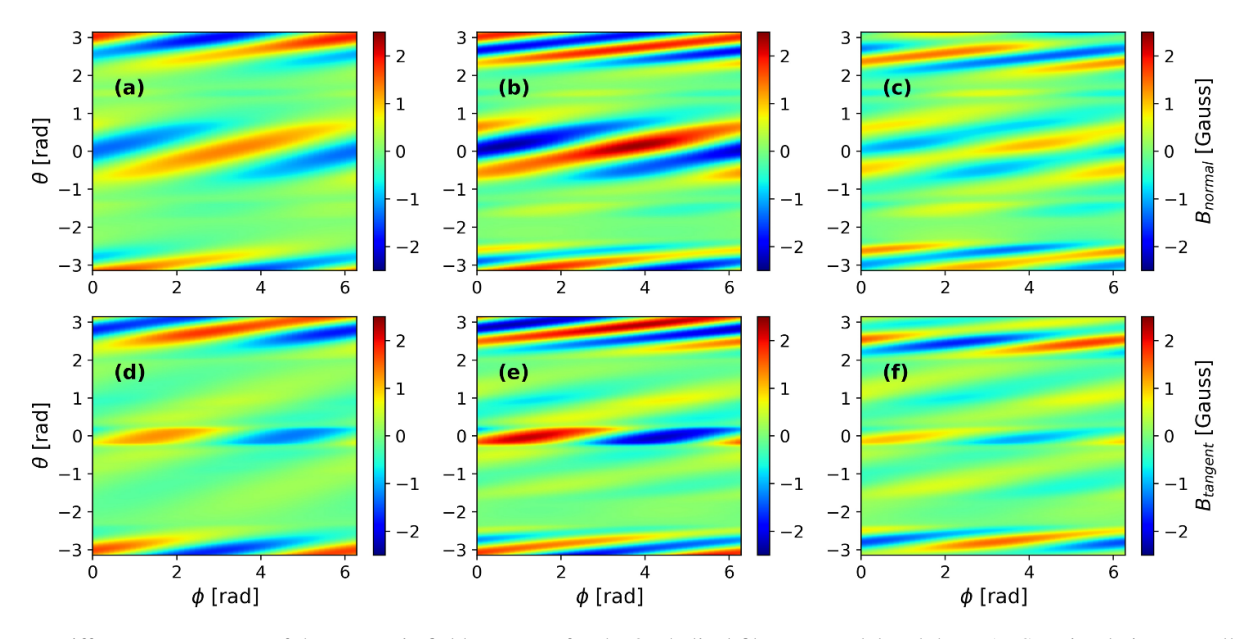


Figure 6. Different components of the magnetic field response for the 3D helical filament model and the MARS-F simulation as well as their residuals for the DIII-D discharge. Specifically, the real components of (a) filament  $B_{\text{normal}}$ , (b) MARS-F  $B_{\text{normal}}$ , (c)  $B_{\text{normal}}$  residual, (d) filament  $B_{\text{tangent}}$ , (e) MARS-F  $B_{\text{tangent}}$ , and (f)  $B_{\text{tangent}}$  residual. The residual is computed by taking the difference of the MARS-F and the filament magnetic field response. The poloidal angle  $\theta = \pm \pi$  corresponds to the high-field side and  $\theta = 0$  corresponds to the low-field side of the tokamak cross-section.

the Fourier toroidal mode decomposition as presented in this work

In the final step of the model procedure, described in Step 5 of section 2, we perform the optimization. Setting up the system described by equation (2), we optimize the currents in all filaments using a least-squares optimization. Based on the discussion above, the maximum rank of the matrix A in equation (2) is equal to the number of rational q-surfaces with a given toroidal mode number n.

Finally, after computing the filament currents, the surrogate model is complete and can be used to compare to data. In these results, we compare to the synthetic data that was used in the optimization—the MARS-F magnetic field response at the resistive wall locations. The comparison between the 3D helical filament model and the MARS-F simulated data is shown in figure 6 for two different field components which are more directly relevant to understanding plasma distortions: the tangential ( $B_{tangent}$ ) and normal ( $B_{normal}$ ) components (to the resistive wall) of the magnetic field response. We present the 2D heatmap where the toroidal angle  $\phi$  is shown horizontally and the poloidal angle  $\theta$  is shown vertically and the left-most column shows the results of the magnetic field response for the sum of all the filaments now with their complex currents, the middle column column shows the MARS-F predicted magnetic field response, and the right column shows the difference. For the  $B_{normal}$  and  $B_{tangent}$  components, the agreement is qualitatively quite good with the MARS-F simulation showing higher intensity but otherwise similar shape agreement. In these comparisons, the MARS-F simulation must be vacuum-subtracted and exclude eddy currents. This removes the influence of the I-coils and the resistive wall, both of which are not present in the 3D helical filament model. In experiments, this will be a challenge since the resistive wall is coupled to the plasma. Future implementations of this algorithm will seek to quantify this effect as a correction but, as a zeroth-order effect, we can consider using a similar vacuum discharge to calculate the magnetic response of the I-coils and resistive wall and subtract out those effects from the plasma discharge.

The right-most panel of figure 6 shows the differences as a 2D heatmap. These differences can be used to calculate an average fractional residual using equation (4). Different permutations of filaments can be used to determine the influence of each individual filament on the overall accuracy of the magnetic field response fit. We vary the number of linearly independent filaments by starting with one located at q = 3 and adding an additional filament for each integer q surface until q = 7. Each additional filament adds more degrees of freedom for the fit and indeed this is reflected in the fractional residuals decreasing as a function of the number of filaments. This trend is shown in figure 7. One point of interest is that as we add additional filaments, the residual is not substantially improving—at most, the value decreases by 10%– 20% when using 3 or more filaments. As a result, when using this model for predictions it is important to always use the largest number of available linearly independent filaments to capture the smallest structures when fitting the magnetic field response.

Alternatively, instead of examining the trend in the residuals with varying numbers of basis filaments, we can instead examine the trend as we retain different components of a singular value decomposition (SVD). In the optimization

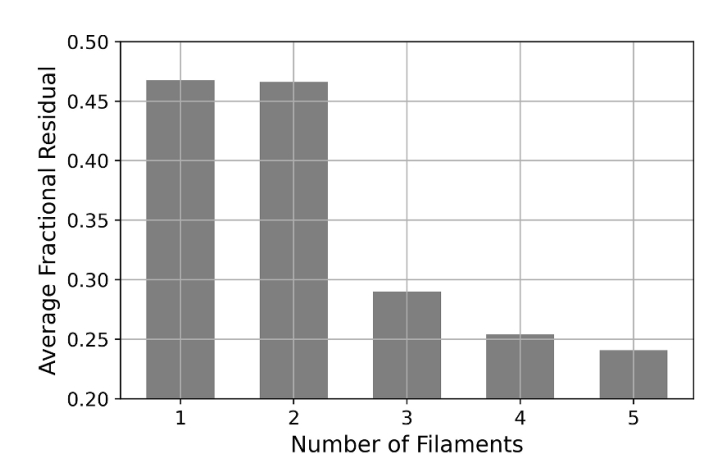


**Figure 7.** Average fractional residual for the different magnetic field components when comparing the optimized 3D helical filament model response to the MARS-F computed response. The average fractional residual is calculated using equation (4). The number of filaments indicate placing incrementally more filaments, starting at q = 3 and adding one at each integer q value up to q = 7.

step shown in equation (2), we can replace the least-squares optimization with the Moore–Penrose pseudoinverse [48]. This version of optimization for x naturally uses an SVD method which is computationally more expensive than leastsquares but provides more information on the singular values (SVs) of the magnetic response matrix A. The SVs can be truncated by zeroing out the lowest value SV. A scan over truncating all the lowest contributing SVs then provides the sensitivity of each helical filament in reconstructing the (reduced) A matrix. The results of such a scan are shown in figure 8. There, we show how the current amplitudes in each filament (labelled sequentially from core to edge) change as different numbers of SVs are truncated from the A matrix. We can see that as the number of SVs change, the core filament amplitudes remain the more constant compared to the edge filament amplitudes, indicating that the core filaments are more robust to the magnetic response. One interpretation of this result is that the core filaments are providing the strongest screening effect, corresponding to the largest shielding current, and therefore producing a dominant field contribution at the probe location. Additionally, the residuals barplot included show that the magnetic response is largely dominated by 2 SVs since the first 3 SV truncation do not significantly impact the residuals. Understanding the filament current optimization under these SVD methods gives a different insight to the physics interpretation of these helical filaments.

The results shown in this section illustrate the application of the 3D helical filament model to a DIII-D discharge with applied RMP modeled by MARS-F to produce synthetic 3D magnetic field data. The results are compared to MARS-F and indicate good agreement. Furthermore, this study identified additional insights into model-order-reduction for linearly dependent filaments and therefore the potential degrees of freedom for such a 3D helical filament model. These

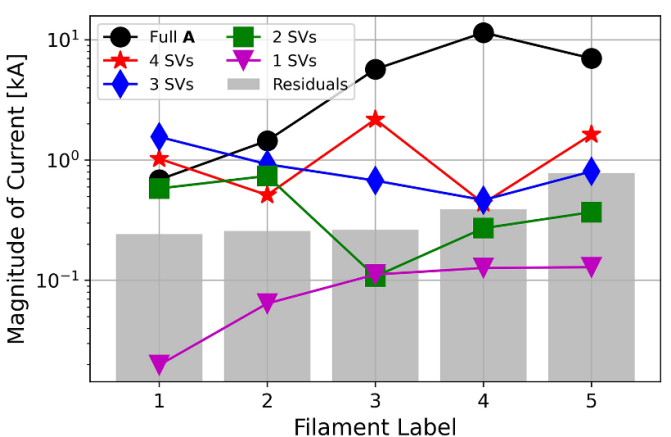


**Figure 8.** Magnitude of the helical filament currents for different realizations of the *A* matrix from equation (2). Specifically, we truncate the lowest-valued singular values (SVs) from an SVD of *A* and show the corresponding filament currents. The filaments are labelled sequentially where 1 corresponds to the inner-most core filament and 5 is the outer-most edge filament (based on starting location for the field-line trace). Overplotted is a barplot that shows the magnitude of the fractional residuals, calculated from equation (4). For the barplot, the horizontal axis instead indicates the number of SVs truncated minus 1 (i.e. the bar labelled '1' has 0 SVs truncated).

promising initial results led us to extend our analysis and apply the same procedure to a MAST-U discharge with different toroidal mode number.

#### 3.2. MAST-U discharge with n = 2 RMP

The Mega Ampere Spherical Tokamak-Upgrade (MAST-U) device is a spherical tokamak located in Culham, UK designed to investigate the burning plasma relevant properties of spherical tokamaks [49, 50] (and references therein). In contrast to DIII-D where the discharge of interest was taken from in the previous section, the spherical aspect ratio of MAST-U allows for lower aspect ratio plasmas and higher q-values to be accessed [51]. One notable difference between the two devices that is relevant for this study is the external RMP coils used for ELM suppression and mitigation. The MAST-U coils themselves are capable of different toroidal mode numbers than in DIII-D and have a different geometric configuration [52]. As a result, the MAST-U discharge will produce different 3D helical filament geometries (and be fit to different magnetic field responses). The MAST-U discharge used in this study is discharge number 45272 at time slice 605 ms (additional discharge and equilibrium quantities presented in [53]).

Emulating the steps in the previous section and outlined in section 2, we start building the filament model using a 2D axisymmetric equilibrium. In this instance, the axisymmetric equilibrium and plasma profiles were obtained by external collaborators and directly used by the MARS-F simulation and filament model construction, highlighting the modular nature of this model procedure.

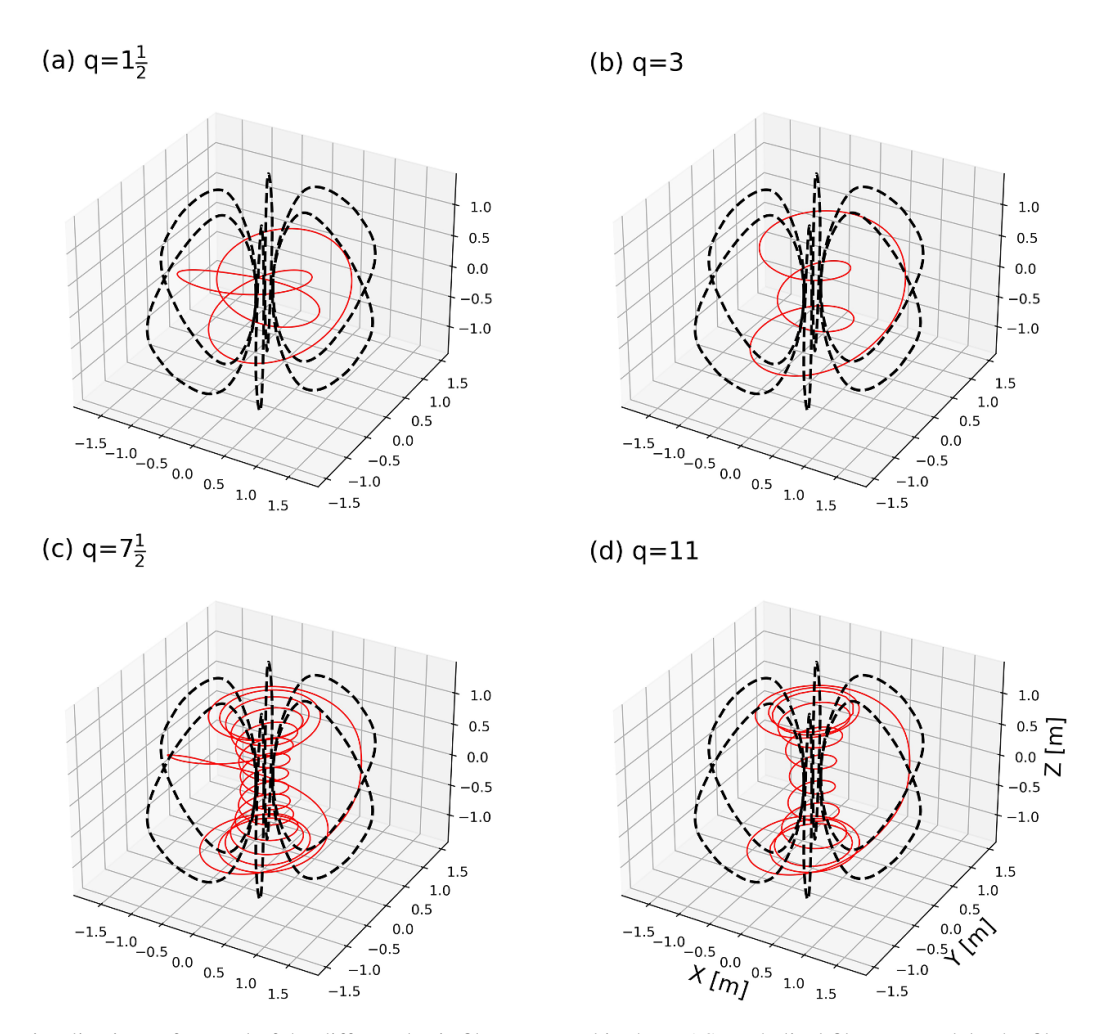


**Figure 9.** 3D visualizations of several of the different basis filaments used in the MAST-U helical filament model. The filament geometry is obtained using REORBIT to perform a field-line trace, starting from a rational q-surface. In each subfigure, we show the geometry (red) corresponding to different q values: (a)  $q = 1\frac{1}{2}$ , (b) q = 3, (c)  $q = 7\frac{1}{2}$ , and (d) q = 11. The resistive wall is shown at six different toroidal slices (dashed black). In contrast to figure 2, there are half-integer q-surface values that form closed geometries due to the choice of toroidal mode number n = 2 for the MAST-U model.

From these equilibrium flux contours, we investigate the model using one filament on each rational q-surface. In this discharge, we set the toroidal mode number n = 2 and given the range of the q-profile, we obtain a total of 21 filaments. They correspond to starting locations at  $q = 1\frac{1}{2}, 2, ..., 11\frac{1}{2}$  in  $\frac{1}{2}$ increments. We show a selected subset of these filament geometries in figure 9. One interesting trend that emerges from these filament geometry traces is that the half integer q-surface filaments show more helicity and overall length before retracing their paths. This indicates that the half-integer q-surface filaments contribute basis functions that may have magnetic field responses that are fairly distinct from the integer qsurface filaments and distinguishes this MAST-U 3D helical filament model from that of the DIII-D discharge. We note that this growth in the number of basis filaments is true for all higher integer values of n as well since there are more fractional q closed filament traces at higher values of n for a given q profile.

Following the model procedure, we optimize the 21 basis filaments using the magnetic field response along the resistive wall. For MAST-U simulations, the resistive wall still consists of 512 points, albeit in a different shape (shown as the dashed contour in figure 9).

We apply this filament model to the phase-shifted magnetic field response of the MAST-U plasma when applying current in the upper and lower RMP coils. Since MARS-F is a linear code, the plasma response of the total RMP coils can be decomposed into the sum of the upper and lower rows of RMP coils with an associated phase shift applied to the field response. In our model, we fit the filament currents to the phase-shifted and summed magnetic field response output by MARS-F. The results of such a comparison between 3D helical filament model and the MARS-F simulation results are shown in figure 10 for the normal and tangential components of the *B*-field only for  $\phi_{\rm UL}=0^{\circ}$ . The filament model shows sharper structures in the field response compared to the

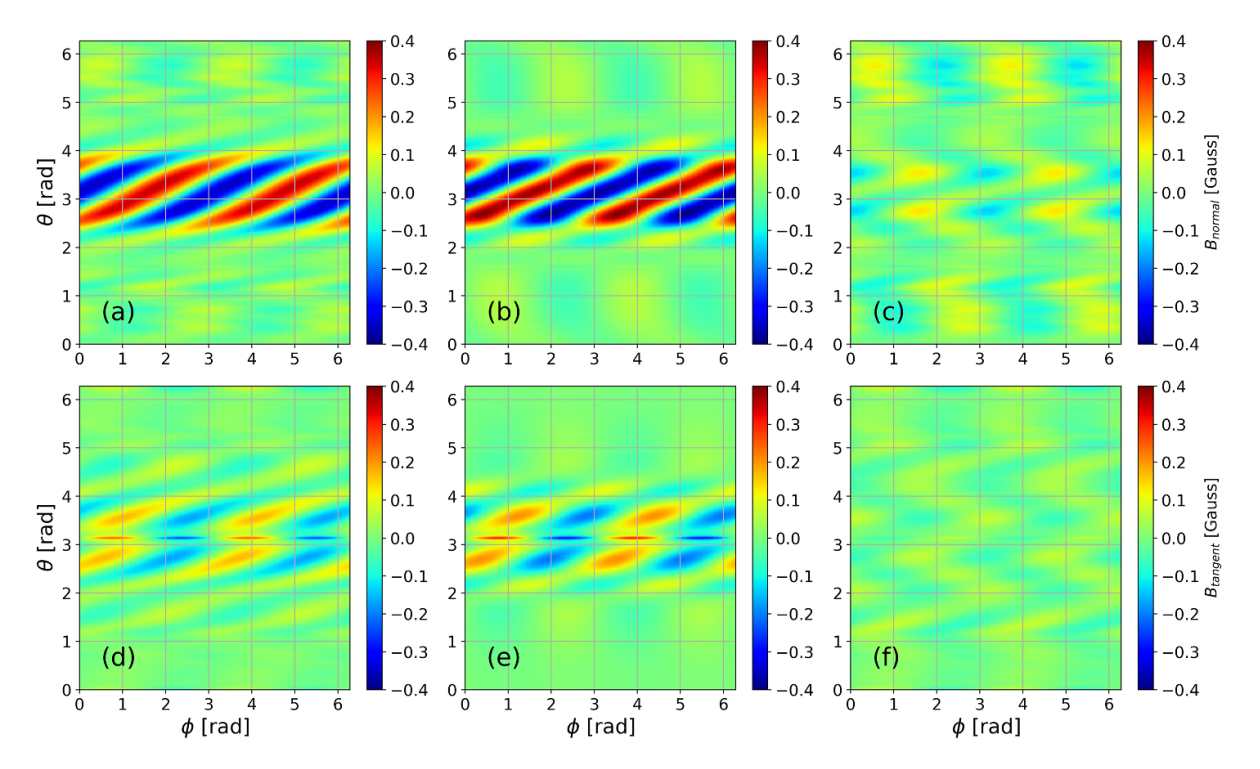


**Figure 10.** Different components of the magnetic field response for the 3D helical filament model and the MARS-F simulation as well as their residuals for the MAST-U discharge, in units of Gauss. Specifically, the real components of (a) filament  $B_{\text{normal}}$ , (b) MARS-F  $B_{\text{normal}}$ , (c)  $B_{\text{normal}}$  residual, (d) filament  $B_{\text{tangent}}$ , (e) MARS-F  $B_{\text{tangent}}$ , and (f)  $B_{\text{tangent}}$  residual. The residual is computed by taking the difference of the MARS-F and the filament magnetic field response. The poloidal angle  $\theta = 0$  corresponds to the high-field side and  $\theta = \pi$  corresponds to the low-field side of the tokamak cross-section.

MARS-F which shows more smooth, lobe structures. But otherwise the magnetic field response between the two follow very similar structures and magnitudes. In the right-most panels (c) and (f), we show the field response from the filament model minus the MARS-F simulation. We note the magnitude of the residuals in these panels is fairly small compared to the magnetic field response (percentage residuals around 30%–40%). As well, the poloidal mode structure of the residuals is clearly larger than that of the filament model or the MARS-F computed response, indicating that the residual difference is due to higher-order effects.

In figure 11, we show the comparison of the normal and tangential component of the magnetic field response for a 90° phase shift between the upper and lower RMP coils. This corresponds to one of the lowest fractional residuals amongst the phase-shifted comparisons and therefore amongst the bestfitting filament models. The horizontal axis shows the poloidal angle  $\theta$  which parametrizes a circular trace around the resistive wall. We see that the structure of the magnetic field response is largely captured by the 3D helical filament model when compared to the MARS-F synthetic data. Most notably, the differences seem to be in small structures near the high-field side of the plasma where the filament model shows more variation and MARS-F computes a smoother magnetic field response. We note that these smaller fluctuations away from the central lobes at the low-field side do still contribute a reasonable amount to the residual values. In addition, the central lobes at the low-field side are well-reproduced by the filament model albeit with more fine structure compared to the 'smoother' MARS-F computed field responses.

We also show the same comparison except for  $\phi_{UL}=270^\circ$  in figure 12. This corresponds to one of the largest fractional residuals and therefore one of the worst-fitting filament models. The main distinction between this comparison and the previous  $\phi_{UL}=90^\circ$  is the parity change of the lobe structure. In figure 11, all the large magnetic field response lobes have odd-parity shapes (evaluated at the low-field side  $\theta=\pi$ ). By comparison, for this phase-shift, the number of lobes have changed (to approximately 4) and all have even-parity shapes. This indicates that the filament model is able to fit different magnetic field responses at varying degrees and potentially the parity change at the low-field side response is relevant in the goodness-of-fit.

Finally, we can repeat our residuals study from the previous section where we vary the number of filaments used in the filament model. We add an additional component to this scan: the phase shift between the upper and lower RMP coil rows. For the number of filaments, we start by placing one filament at the outermost rational q-surface,  $q=11\frac{1}{2}$ , and incrementally adding filaments closer to the core at  $q=1\frac{1}{2}$ . The scan across two different parameters is shown in figure 13. One interesting trend in this scan is the phase dependence of the residuals. For certain phase shifts, typically around  $90^{\circ}$ , the filaments have lower residuals and hence a higher fidelity fit to the MARS-F synthetic data. Closer examination of the 2D heatmap magnetic field response indicates that this is

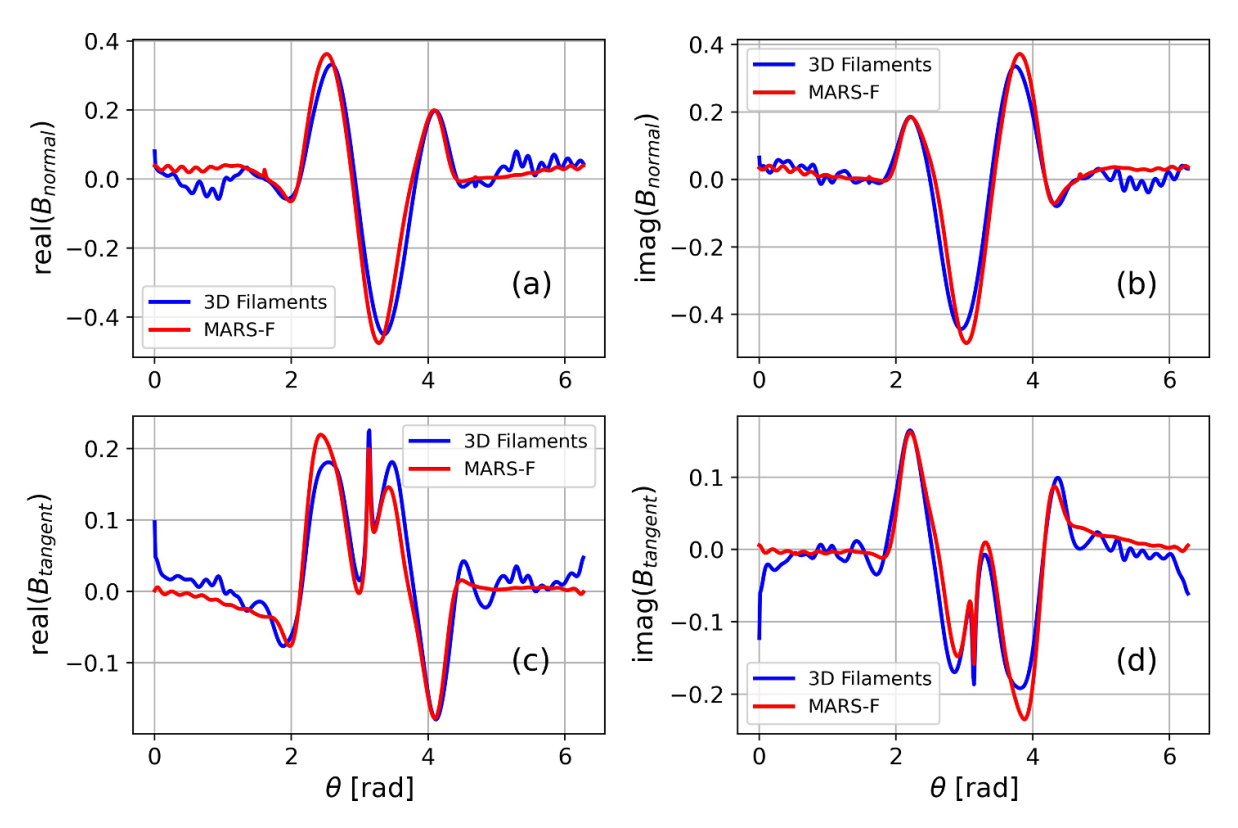


**Figure 11.** Profiles of the different components of the magnetic field response for the 3D helical filament model and the MARS-F response for the MAST-U discharge. We show (a) real component of  $B_{\text{normal}}$ , (b) imaginary component of  $B_{\text{normal}}$ , (c) real component of  $B_{\text{tangent}}$ , and (d) imaginary component of  $B_{\text{tangent}}$ . The phase shift of the summed upper and lower RMP coil response in MARS-F is  $\phi_{\text{UL}} = 90^{\circ}$ . These profiles are approximately a minimum in the average fractional residuals.

due to the phase-shifted MARS-F plasma response containing microstructures that look more 'filamentary' and so the helical filaments are better able to approximate the response.

The results of this section apply and further extend the 3D helical filament model to a different parameter space by using a different tokamak discharge. Namely, for a MAST-U discharge of different RMP toroidal mode number, we find the helical filament model is still able to accurately reconstruct the magnetic field response. Furthermore, interesting trends emerge where the phase-shift of the applied RMP coils influence the overall goodness of fit of the filament model.

## 4. Conclusion

Modern day tokamaks rely on 2D axisymmetric equilibrium reconstructions for much of their understanding of the underlying plasma state, both in real-time control and for off-line analysis. It is known that 3D perturbations are a regular occurrence that are not captured by the 2D axisymmetric assumption. Furthermore, 3D effects are particularly relevant in burning plasma device operation due to 3D distortions potentially signaling disruptions, or for the application of 3D perturbations that are used in modern tokamak operations. In particular, next-generation burning plasma devices need to be robust to disruptions and better understanding of 3D equilibrium reconstructions can assist this objective. The 3D helical

filament model for 3D equilibrium reconstructions described in this work aims to help resolve this issue.

In this work, we presented the algorithm/procedure for developing a 3D helical filament model capable of producing a surrogate model for 3D equilibrium reconstructions. We outline the steps for constructing this model and applied it to one type of use-case: the RMP. We compare the 3D helical filament model to the synthetic 3D plasma distortions predicted by MARS-F when an RMP is applied. This was done for two different discharges: a toroidal mode number n = 1discharge from DIII-D and an n = 2 discharge from MAST-U. We present the comparisons between the simulated 3D magnetic field response from MARS-F and the best-fit 3D helical filament model and obtain good agreement with average fractional residuals for the B-field response of approximately 20%. In addition, we present two insights obtained throughout the course of this initial development of the model. First, we highlight that the helical filaments as prescribed in this work produce identical magnetic field response up to a toroidal rotation if the filaments originate on the same rational q-surface. This implies that there is a maximum number of linearly independent basis functions that can be used in the 3D helical filament model and it is related to the accessible q-profile. Second, when modeling the phase-shifted magnetic field response due to the application of RMPs from upper and lower RMP coils, the goodness-of-fit is dependent on the phase

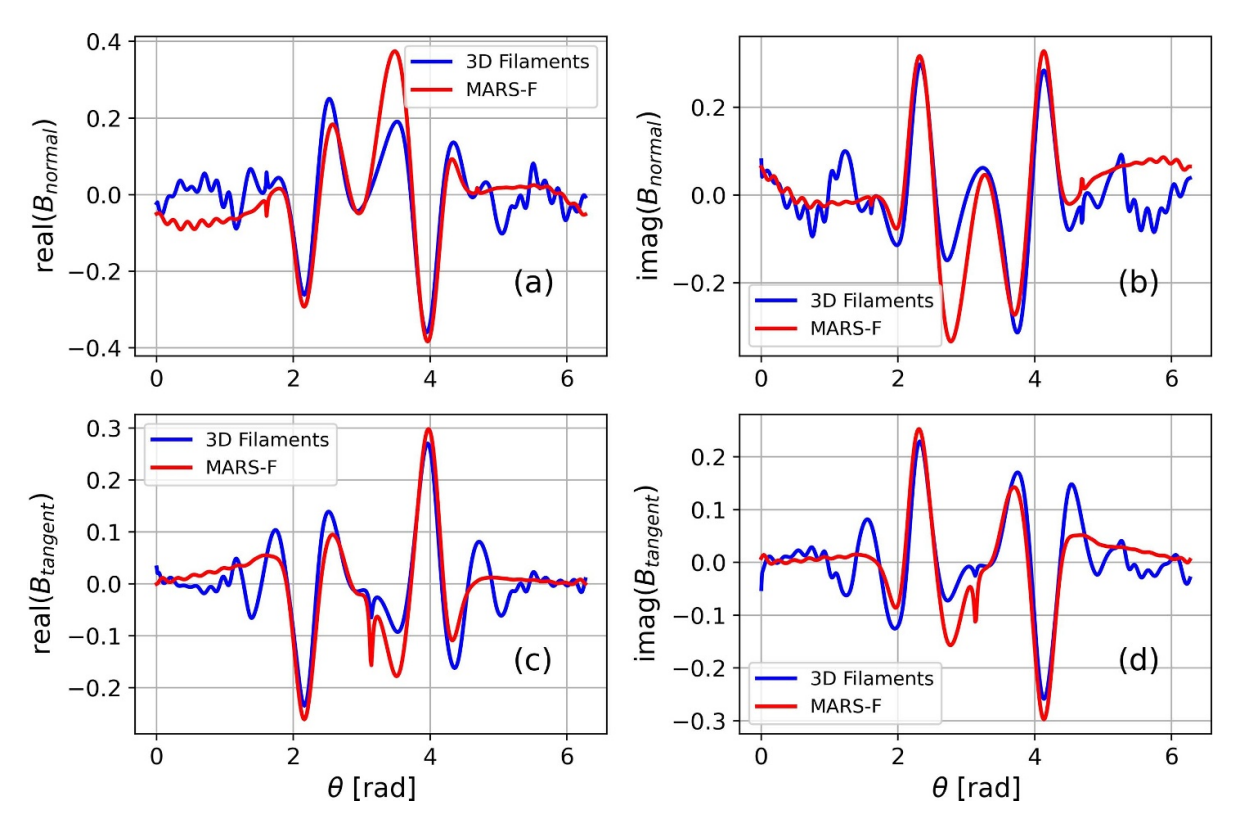


**Figure 12.** Profiles of the different components of the magnetic field response for the 3D helical filament model and the MARS-F response for the MAST-U discharge. We show (a) real component of  $B_{\text{normal}}$ , (b) imaginary component of  $B_{\text{normal}}$ , (c) real component of  $B_{\text{tangent}}$ , and (d) imaginary component of  $B_{\text{tangent}}$ . The phase shift of the summed upper and lower RMP coil response in MARS-F is  $\phi_{\text{UL}} = 270^{\circ}$ . These profiles are approximately a maximum in the average fractional residuals.

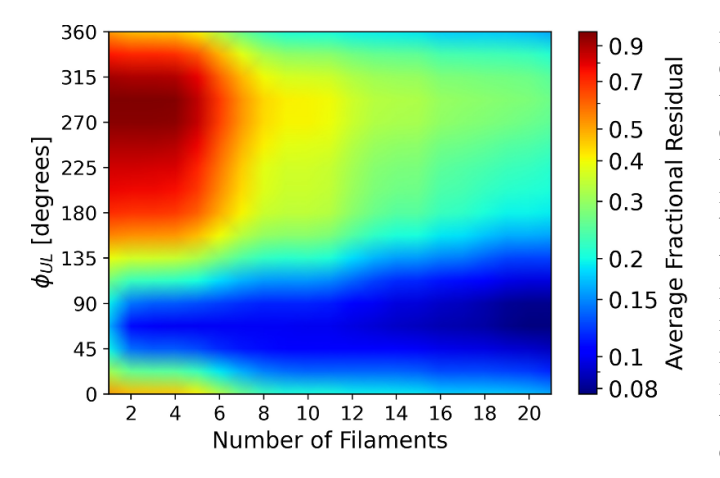


**Figure 13.** Sensitivity study showing the average fractional residual vs the upper and lower RMP coil phasing and the number of filaments included in the 3D helical filament model. The number of filaments starts with one placed at  $q=11\frac{1}{2}$  and incrementally adds filaments at each  $\Delta q=\frac{1}{2}$  until  $q=1\frac{1}{2}$ . The calculation of the average fractional residual is given in equation (4).

shift. More specifically, the fractional residuals of the filament model show a phase-shift dependency.

The initial results and development of this 3D helical filament model for 3D equilibrium reconstruction have been promising. An algorithm was investigated that is scalable to

massively parallel speeds. Predictions seem to agree well with existing, validated 3D MHD codes such as MARS-F. And the framework for extending this surrogate model has been established. Future work on this surrogate model aims to continue extending the capabilities. In particular, we would like to investigate additional, disruption-relevant quantities that may be influential 3D precursors to disruptions. In addition, we aim to transition away from 3D simulation data with real magnetic probe measurements. This has the added benefit of allowing analysis on magnetic field responses with a toroidal mode number n distribution since the magnetic probes and the filament response are not restricted to specific mode number solutions. The study using real magnetic probe data will be beneficial as well for probing the question of data scarcity. Namely, a minimum number of magnetic probes with a given toroidal distribution must be present or else the filament model does not have enough data to accurately fit for the current amplitudes and phases. In this proof-of-principle study, we were able to obtain good fits since the MARS-F response can be interrogated in any 3D location. We expect in the next stage of development that investigating the spatial distribution of magnetic probes (as well as number) will make a significant impact on the performance of the model, especially in experimental contexts. Finally, we note that the current development of the model has proceeded in many stages with different components as needed: the equilibrium reconstruction, the fieldline tracing module (which was chosen to be REORBIT but can be replaced with any other integrated code), and more. Future developments aims to tightly integrate these disjoint codes under the goal of providing a package that can construct this model for real-time deployment by interfacing the different components of this model construction for the fastest computation speeds.

#### Data availability statement

All data that support the findings of this study are included within the article (and any supplementary files).

#### **Acknowledgment**

This material is based upon work supported by General Atomics internal funding and by the U.S. Department of Energy, Office of Science, Office of Fusion Energy Sciences under award numbers DE-SC0018992, DE-SC0021203, DE-FG02-95ER54309, and DE-FC02-04ER54698 and using the DIII-D National Fusion Facility, a DOE Office of Science user facility. This work has been part-funded by the EPSRC Energy Programme [Grant Number EP/W006839/1].

#### Disclaimer

This report was prepared as an account of work sponsored by an agency of the United States Government. Neither the United States Government nor any agency thereof, nor any of their employees, makes any warranty, express or implied, or assumes any legal liability or responsibility for the accuracy, completeness, or usefulness of any information, apparatus, product, or process disclosed, or represents that its use would not infringe privately owned rights. Reference herein to any specific commercial product, process, or service by trade name, trademark, manufacturer, or otherwise, does not necessarily constitute or imply its endorsement, recommendation, or favoring by the United States Government or any agency thereof. The views and opinions of authors expressed herein do not necessarily state or reflect those of the United States Government or any agency thereof.

## **ORCID iDs**

Xuan Sun https://orcid.org/0000-0001-8817-4643
Yueqiang Liu https://orcid.org/0000-0002-8192-8411
Lang L Lao https://orcid.org/0000-0003-1937-2675
Nathan Richner https://orcid.org/0000-0001-5544-3915
David Ryan https://orcid.org/0000-0002-7735-3598
Guoliang Xia https://orcid.org/0009-0009-4236-077X

#### References

[1] Lao L L, John H E Peng J Q, Ferron J R, Strait E J, Taylor T S, Meyer W H, Zhang C and You K I 2005 MHD equilibrium reconstruction in the DIII-D tokamak *Fusion Sci. Technol.* 48 968–77

- [2] Jinping Q et al 2009 Equilibrium reconstruction in EAST tokamak Plasma Sci. Technol. 11 142–5
- [3] O'Brien D P, Lao L L, Solano E R, Garribba M, Taylor T S, Cordey J G and Ellis J J 1992 Equilibrium analysis of iron core tokamaks using a full domain method *Nucl. Fusion* 32 1351–60
- [4] Sabbagh S A et al (NSTX Research Team) 2001 Equilibrium properties of spherical torus plasmas in NSTX Nucl. Fusion 41 1601–11
- [5] Park Y S et al 2011 KSTAR equilibrium operating space and projected stabilization at high normalized beta Nucl. Fusion 51 053001
- [6] Grad H and Rubin H 1958 Hydromagnetic equilibria and force-free fields *Technical Report* Institute of Mathematical Sciences, United Nations (UN) INIS-XU-021
- [7] Shafranov V D 1966 Plasma equilibrium in a magnetic field Rev. Plasma Phys. 2 103
- [8] Lao L L, St H Stambaugh J R D, Kellman A G and Pfeiffer W 1985 Reconstruction of current profile parameters and plasma shapes in tokamaks *Nucl. Fusion* 25 1611–22
- [9] Swain D W and Neilson G H 1982 An efficient technique for magnetic analysis of non-circular, high-beta tokamak equilibria Nucl. Fusion 22 1015
- [10] Lao L L, John H Stambaugh J R D and Pfeiffer W 1985 Separation of  $\bar{\beta}_p$  and  $l_i$  in tokamaks of non-circular cross-section *Nucl. Fusion* **25** 1421
- [11] Evans T E *et al* 2006 Edge stability and transport control with resonant magnetic perturbations in collisionless tokamak plasmas *Nat. Phys.* **2** 419–23
- [12] Hirshman S P and Whitson J C 1983 Steepest-descent moment method for three-dimensional magnetohydrodynamic equilibria *Phys. Fluids* 26 3553–68
- [13] Hanson J D, Hirshman S P, Knowlton S F, Lao L L, Lazarus E A and Shields J M 2009 V3FIT: a code for three-dimensional equilibrium reconstruction *Nucl. Fusion* 49 075031
- [14] Spong D A et al 2001 Physics issues of compact drift optimized stellarators Nucl. Fusion 41 711
- [15] Suzuki Y, Nakajima N, Watanabe K, Nakamura Y and Hayashi T 2006 Development and application of HINT2 to helical system plasmas *Nucl. Fusion* 46 L19
- [16] Park J-K, Boozer A H and Glasser A H 2007 Computation of three-dimensional tokamak and spherical torus equilibria *Phys. Plasmas* 14 052110
- [17] Park J-K and Logan N C 2017 Self-consistent perturbed equilibrium with neoclassical toroidal torque in tokamaks *Phys. Plasmas* 24 032505
- [18] Lazerson S A (The DIII-D Team) 2015 Three-dimensional equilibrium reconstruction on the DIII-D device *Nucl.* Fusion 55 023009
- [19] Merkel P 1987 Solution of stellarator boundary value problems with external currents *Nucl. Fusion* 27 867
- [20] Zhu C, Hudson S R, Song Y and Wan Y 2020 Erratum: new method to design stellarator coils without the winding surface (2018 Nucl. Fusion 58 016008) Nucl. Fusion 60 089601
- [21] Wingen A, Evans T E, Lasnier C J and Spatschek K H 2010 Numerical modeling of edge-localized-mode filaments on divertor plates based on thermoelectric currents *Phys. Rev. Lett.* 104 175001
- [22] Wingen A, Evans T E and Spatschek K H 2011 Effect of thermoelectric current splitting on the magnetic topology in DIII-D Phys. Plasmas 18 042501
- [23] Rack M, Wingen A, Liang Y, Spatschek K H, Harting D M and Devaux S 2012 Thermoelectric currents and their role during ELM formation in JET Nucl. Fusion 52 074012
- [24] Rack M et al (The EAST Team) 2014 Modelling of LHW-induced helical current filaments on EAST: study of

- an alternative method of applying RMPs *Nucl. Fusion* **54** 064016
- [25] Liu Y, Akcay C, Lao L L and Sun X 2022 Surrogate models for plasma displacement and current in 3D perturbed magnetohydrodynamic equilibria in tokamaks *Nucl. Fusion* 62 126067
- [26] Zohm H 1996 Edge localized modes (ELMs) Plasma Phys. Control. Fusion 38 105
- [27] Loarte A et al 2014 Progress on the application of ELM control schemes to ITER scenarios from the non-active phase to DT operation Nucl. Fusion 54 033007
- [28] Kirk A et al 2013 Understanding the effect resonant magnetic perturbations have on ELMs Plasma Phys. Control. Fusion 55 124003
- [29] He K, Pan C and Feng K 2002 An overview on plasma disruption mitigation and avoidance in tokamak
- [30] Zakharov L E, Galkin S A and Gerasimov S N (JET-EFDA contributors) 2012 Understanding disruptions in tokamaks *Phys. Plasmas* 19 055703
- [31] Eidietis N W 2021 Prospects for disruption handling in a tokamak-based fusion reactor *Fusion Sci. Technol*. 77 738–44
- [32] Choi M J, Park H K, Yun G S, Lee W, Luhmann N C, Lee K D, Ko W-H, Park Y-S, Park B H and In Y 2016 In 2D/3D electron temperature fluctuations near explosive MHD instabilities accompanied by minor and major disruptions *Nucl. Fusion* 56 066013
- [33] Strauss H, Paccagnella R, Breslau J, Sugiyama L and Jardin S 2013 Sideways wall force produced during tokamak disruptions *Nucl. Fusion* 53 073018
- [34] Liu Y Q, Bondeson A, Fransson C M, Lennartson B and Breitholtz C 2000 Feedback stabilization of nonaxisymmetric resistive wall modes in tokamaks. I. Electromagnetic model *Phys. Plasmas* 7 3681–90
- [35] Sun X, Liu Y, Lao L, Paz-Soldan C and Milliano J 2024 Validation of MARS-F modeling of plasma response to RMPs using internal measurements on DIII-D *Phys. Plasmas* 31 013902
- [36] Liu Y, Connor J W, Cowley S C, Ham C J, Hastie R J and Hender T C 2012 Continuum resonance induced electromagnetic torque by a rotating plasma response to static resonant magnetic perturbation field *Phys. Plasmas* 19 102507
- [37] Reiman A *et al* 2015 Tokamak plasma high field side response to an n = 3 magnetic perturbation: a comparison of 3D equilibrium solutions from seven different codes *Nucl. Fusion* **55** 063026
- [38] Liu Y Q, Parks P B, Paz-Soldan C, Kim C and Lao L L 2019 MARS-F modeling of post-disruption runaway beam loss

- by magnetohydrodynamic instabilities in DIII-D *Nucl. Fusion* **59** 126021
- [39] Luxon J L et al 1990 Recent results from DIII-D and their implications for next generation tokamaks Plasma Phys. Control. Fusion 32 869
- [40] Allen S L (D-D DIII-D Team) 2001 Overview of recent experimental results from the DIII-D advanced tokamak programme Nucl. Fusion 41 1341
- [41] Buttery R J *et al* 2019 DIII-D research to prepare for steady state advanced tokamak power plants *J. Fusion Energy* 38 72–111
- [42] King J D et al 2015 Experimental tests of linear and nonlinear three-dimensional equilibrium models in DIII-D Phys. Plasmas 22 072501
- [43] Meneghini O *et al* 2015 Integrated modeling applications for tokamak experiments with OMFIT *Nucl. Fusion* **55** 083008
- [44] Seraydarian R P, Burrell K H, Brooks N H, Groebner R J and Kahn C 1986 Multichordal charge exchange recombination spectroscopy on the Doublet III tokamak *Rev. Sci. Instrum.* 57 155–63
- [45] Isler R C 1994 An overview of charge-exchange spectroscopy as a plasma diagnostic *Plasma Phys. Control. Fusion* 36 171
- [46] Strait E J 2006 Magnetic diagnostic system of the DIII-D tokamak Rev. Sci. Instrum. 77 023502
- [47] King J D et al 2014 An upgrade of the magnetic diagnostic system of the DIII-D tokamak for nonaxisymmetric measurements Rev. Sci. Instrum. 85 083503
- [48] Golan. J S 1995 The Moore-Penrose Pseudoinverse (Springer) pp 198–203
- [49] Lloyd B et al (The MAST and NBI Teams) 2003 Overview of recent experimental results on MAST Nucl. Fusion 43 1665
- [50] Harrison J R et al (The MAST-U Team and the EUROfusion MST1 Team) 2019 Overview of new MAST physics in anticipation of first results from MAST Upgrade Nucl. Fusion 59 112011
- [51] Peng Y-K M 2000 The physics of spherical torus plasmas Phys. Plasmas 7 1681–92
- [52] Ryan D A et al (The MAST Upgrade Team and the EUROfusion Tokamak Exploitation Team) 2024 First observation of RMP ELM mitigation on MAST Upgrade Plasma Phys. Control. Fusion 66 105003
- [53] Munaretto S, Liu Y Q, Ryan D A, Hao G Z, Berkery J W, Blackmore S and Kogan L 2024 Chasing the multi-modal plasma response in MAST-U *Plasma Phys. Control. Fusion* 66 065023